


Successive magnetic phase transitions with magnetoelastic and magnetodielectric coupling in the ordered triple perovskite $\text{Sr}_3\text{CaRu}_2\text{O}_9$

Arun Kumar¹, Pascal Manuel², and Sunil Nair¹

¹*Department of Physics, Indian Institute of Science Education and Research, Dr. Homi Bhabha Road, Pune, Maharashtra 411008, India*

²*ISIS Pulsed Neutron Source, STFC Rutherford Appleton Laboratory, Didcot, Oxfordshire OX11 0QX, United Kingdom*

 (Received 19 July 2023; revised 3 January 2024; accepted 19 January 2024; published 13 February 2024)

We report a comprehensive temperature-dependent investigation of the 1:2 ordered triple perovskite system $\text{Sr}_3\text{CaRu}_2\text{O}_9$. It crystallizes in the monoclinic structure with space group $P2_1/c$, consisting of corner-sharing CaO_6 and RuO_6 octahedra. Using dc magnetization and neutron diffraction measurements, we show that this system undergoes successive magnetic transitions at ~ 190 and ~ 160 K. From the analysis of the temperature-dependent neutron diffraction and dielectric data, we demonstrate two distinguishing features of the $\text{Sr}_3\text{CaRu}_2\text{O}_9$ system: (i) magnetoelastic coupling associated with the two magnetic transitions, as revealed by a change in the unit cell volume, direct Ru-Ru distance, and bond angles and (ii) magnetodielectric coupling, as revealed by the anomalies across the two magnetic transitions. The present results would add significantly to the current understanding of the triple perovskites with incipient spin-orbit coupling.

DOI: [10.1103/PhysRevMaterials.8.024405](https://doi.org/10.1103/PhysRevMaterials.8.024405)

I. INTRODUCTION

The $3d$ transition metal-based perovskite oxides have continued to occupy a prominent place in the area of strongly correlated systems. In the recent past, the study of hybrid $3d - 4d/5d$ transition metal oxide-based triple perovskites with the general formula $A_3BB'_2\text{O}_9$ (where $A = \text{Ba}, \text{Sr}$ and $B = \text{Ru}, \text{Ir}, \text{Os}, \text{Nb}, \text{Ta}, \text{Sb}$) has become a very active area of research due to their wide-ranging functional properties with potential for technological applications [1–13]. The intricate interplay between the strong spin-orbit coupling, electronic correlations, crystal field effects and Hund's coupling in such perovskites [1] lead to novel electronic and magnetic properties such as Mott insulators [2], quantum spin-liquids [3–5], quantum spin-orbital liquid [6], spin-glass [7], long-range antiferromagnetic (AFM) [8,9] /ferromagnetic (FM) ordering [10,11] and multiferroicity [12,13].

Within the triple perovskites, Ba-based triple perovskite ruthenates and iridates of the form $\text{Ba}_3\text{BB}'_2\text{O}_9$ ($B = \text{alkali metals}, \text{alkaline earth metals}, \text{or lanthanides}$ and $B' = \text{Ru}, \text{Ir}$) have been widely investigated for their structure-property correlations [9–11,14–19]. Most derivatives usually adopt the aristotype $6H$ -hexagonal structure in which Ba ion occupies the 12-fold-coordinated site while B and B' occupy the corner and face-shared sites, respectively, forming BO_6 octahedra and $\text{B}'_2\text{O}_9$ dimers comprising of two face-shared $\text{B}'\text{O}_6$ octahedra. Interestingly, the $\text{B}'_2\text{O}_9$ dimer units arranged along the c axis produce a triangular lattice of B' atoms in the a - b plane. Based on such structural features and choice of non-magnetic or magnetic B cations, these triple perovskite oxides exhibit diverse structural as well as magnetic phenomena such as spin dimer [14], spin-gap opening [15,16], charge ordering [17], long-range AFM ordering [9–11], magnetostructural transitions [9,18], magnetoelastic coupling [16], and magnetodielectric coupling [19,20].

In contrast, the investigation of Sr-based triple perovskites of the form $\text{Sr}_3\text{BB}'_2\text{O}_9$ has been limited to a few systems [5,8,21,22]. These Sr analogs are characterized by monoclinic symmetry in which B and B' cations form corner-sharing BO_6 and $\text{B}'\text{O}_6$ octahedra and feature a unique buckled honeycomb lattice of B' atoms. Among the family of Sr-based triple perovskites, $\text{Sr}_3\text{CaRu}_2\text{O}_9$ is particularly interesting, as it was the first compound to exhibit a 1:2 cation ordering at the B site in transition metals with partially filled d orbitals [23] in contrast to earlier reported d^0 cations (nonmagnetic) like Nb^{5+} , Ta^{5+} [24]. To the best of our knowledge, no detailed (magnetic, dielectric or transport) investigations were carried out on $\text{Sr}_3\text{CaRu}_2\text{O}_9$, except the room temperature crystal structure [23]. It is of interest to investigate $\text{Sr}_3\text{CaRu}_2\text{O}_9$ to better understand the structure-property correlations in the family of triple perovskite ruthenates. The two Sr-based 5d triple perovskites $\text{Sr}_3\text{CaIr}_2\text{O}_9$ and $\text{Sr}_3\text{CaOs}_2\text{O}_9$ have been investigated in the past for their room-temperature crystal structure and magnetic properties [8,21]. Both are reported to crystallize in the monoclinic structure in the $P2_1/c$ space group but exhibit different magnetic behavior [8,21]. The $\text{Sr}_3\text{CaIr}_2\text{O}_9$ shows paramagneticlike behavior below room temperature [21], while $\text{Sr}_3\text{CaOs}_2\text{O}_9$ exhibits long-range ordered antiferromagnetic (AFM) transition with $T_N \sim 385$ K [8] which is the highest among all the members of the triple perovskites family. Theoretically, it has been argued that the sizeable antiferromagnetic exchange interaction between the puckered planes results in a high T_N [8].

Here, we report on $\text{Sr}_3\text{CaRu}_2\text{O}_9$, a hitherto unexplored member of the triple perovskite family, using a combination of x-ray diffraction, neutron powder diffraction, dc magnetization, specific heat, dielectric, and resistivity measurements. It is shown that $\text{Sr}_3\text{CaRu}_2\text{O}_9$ crystallizes in the monoclinic symmetry with $P2_1/c$ space group. Temperature-dependent dc magnetization and neutron diffraction analysis

reveal two magnetic transitions, ~ 160 and ~ 190 K, below room temperature. Further, the temperature dependent dielectric permittivity also exhibits anomalies across the two magnetic transitions suggesting the possibility of magnetodielectric coupling.

II. EXPERIMENTAL DETAILS

Single-phase polycrystalline specimens of $\text{Sr}_3\text{CaRu}_2\text{O}_9$ (SCRO) were synthesized by the conventional solid-state method using high-purity carbonates SrCO_3 ($\geq 99.999\%$, Sigma Aldrich), CaCO_3 ($\geq 99.95\%$, Sigma Aldrich) and oxide RuO_2 ($\geq 99.9\%$, Sigma Aldrich) as starting materials. Stoichiometric amounts of precursor powders were thoroughly ground for 6 h in an agate mortar and pestle with ethanol as a mixing medium. The homogeneously mixed powder was first calcined at 1123 K for 12 h in air, followed by re-calcination at 1473 K twice for 48 h each with intervening regrinding. Subsequently, the calcined powder was pressed into pellets (13 mm diameter and 1.0 mm thickness) and sintered at 1498 K for 12 h. The pellets were crushed into a fine powder and then annealed at 773 K for 12 h to remove the strain produced during crushing. The well-annealed powder was used for the x-ray diffraction and neutron scattering measurements.

The elemental compositions were checked by the energy dispersive x-ray (EDS) spectroscopic technique attached with field emission scanning electron microscope (Model-Zeiss Ultra Plus). X-ray diffraction (XRD) measurements were performed using a high-resolution powder diffractometer operated in the Bragg-Brentano geometry (Bruker, Model-D8 ADVANCE) with $\text{Cu-K}\alpha$ radiation, wavelength $\lambda \sim 1.5406 \text{ \AA}$. Temperature and field-dependent dc magnetization measurements were carried out using a superconducting quantum interference device-based magnetometer (MPMS-XL, Quantum Design, USA). Temperature-dependent heat capacity was measured by the relaxation method using a physical property measurement system (PPMS, Quantum Design, USA). Temperature-dependent resistivity measurements were carried out using the four-probe method in the same PPMS. Temperature-dependent dielectric measurements were performed using a close-cycle refrigerator system and a Novocontrol (Model-Alpha-A) high-performance frequency analyzer. Temperature-dependent time-of-flight neutron diffraction experiments were performed using the WISH diffractometer at ISIS Facility, UK [25]. The powder sample was loaded into a 6-mm-diameter cylindrical vanadium can and mounted within a ^4He cryostat. Neutron diffraction patterns were collected from a base temperature of 1.5 up to 250 K, in 10 K steps. The XRD and neutron diffraction data were analyzed by the Rietveld refinement technique using FULLPROF software [26]. The crystal and magnetic structures were drawn using the VESTA software [27].

III. RESULTS AND DISCUSSION

The average atomic percentage ratio determined by the EDS analysis Sr: Ca: Ru $\approx (2.93 \pm 0.05): (0.99 \pm 0.05): (2.10 \pm 0.06)$ are very close to the nominal compositions, confirming the excellent quality of our sample. The crystal structure of SCRO was analyzed by laboratory XRD, and

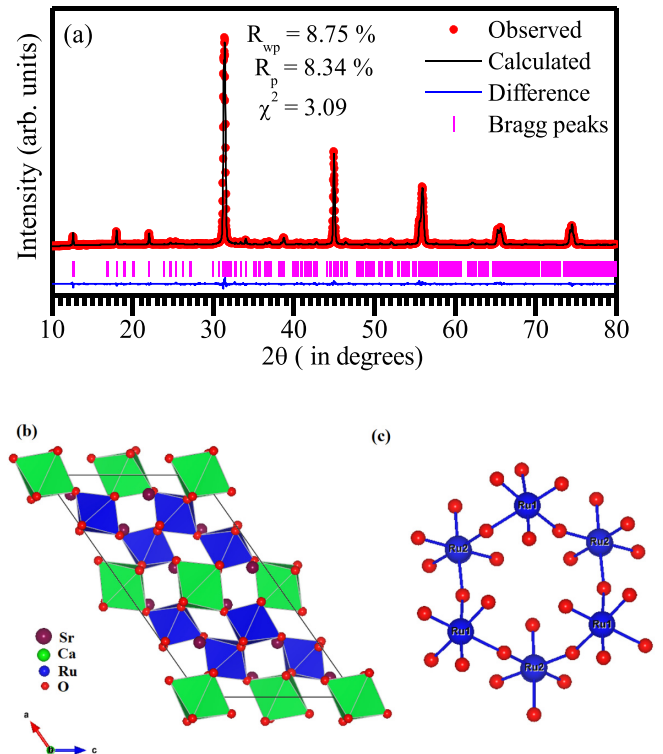


FIG. 1. (a) shows the observed (filled red circles), calculated (continuous black line) and difference (bottom blue line) profiles obtained after Rietveld refinement of x-ray powder diffraction data using the monoclinic $P2_1/c$ space group at 300 K for $\text{Sr}_3\text{CaRu}_2\text{O}_9$. The vertical tick marks (pink color) indicate the expected Bragg peak positions. (b) depicts the schematic crystal structure of $\text{Sr}_3\text{CaRu}_2\text{O}_9$, where wine, green, blue and red color balls represent the Sr^{2+} , Ca^{2+} , Ru^{5+} and O^{2-} , respectively. It can be viewed as a 1:2 ordered structure with stacking sequence of one layer of CaO_6 octahedra and two layers of RuO_6 octahedra along the $[101]$ direction. (c) represents a buckled honeycomb lattice formed by the Ru-atoms.

the room temperature XRD pattern is shown in Fig. 1(a). Analysis of the XRD pattern confirms the single-phase formation without any impurity phase. All the peaks could be indexed with the monoclinic phase in the $P2_1/c$ space group, as confirmed by the Rietveld refinement technique. The supercell of the SCRO consists of 16 independent atoms, all of which occupy the general positions except for two Ca ions which are fixed at the special positions. In the refinements, the background was modeled using linear interpolation between the data points. The peak shape was modeled using a pseudo-Voigt function. The full-width at half-maxima (FWHM) of the peaks were modeled using the Caglioti equation [28] $(\text{FWHM})^2 = U \tan^2 \theta + V \tan \theta + W$. During the refinement, scale factor, zero displacement, lattice parameters (a , b , c), atomic coordinates (x , y , z) and thermal parameters (B) were allowed to vary. Figure 1(a) depicts the observed (red-filled circles) and calculated (black continuous line) XRD profiles of SCRO for the monoclinic $P2_1/c$ space group. Both profiles show excellent fit as can be seen from the nearly smooth difference profile shown in the bottom line (blue continuous line) of the same figure. Table S1 of the Supplemental Mate-

rial [29] summarizes the structural parameters of SCRO after the Rietveld refinement using $P2_1/c$ space group which agree well with the values reported in the literature [23].

We have also attempted to refine the structure of SCRO by considering anti site disorder where Ca and Ru occupancies are treated as variables. Attempts to refine the occupancy did not improve the fits. The occupancies were fixed to the nominal composition. There is no evidence for the presence of antisite disorder in SCRO within the limits of Rietveld analysis. In contrast, a small (3–5%) antisite disorder between Ca and Os sites have been reported in the triple perovskite $\text{Sr}_3\text{CaOs}_2\text{O}_9$ system [8].

A schematic crystal structure of SCRO is shown in Fig. 1(b), which can be described as 1:2 ordering of Ca^{2+} and Ru^{5+} cations over the six coordinated B site of the perovskite where the CaO_6 octahedra are corner shared with RuO_6 octahedra and Sr^{2+} cations occupying the 12-fold coordinated A site. It can also be visualized as a layered structure with stacking sequence of (one layer of) CaO_6 octahedra and (two layers of) RuO_6 octahedra along the crystallographic $[101]$ direction. The 1:2 cation ordering is driven by significant charge and size difference between Ca^{2+} (1.00 Å) and Ru^{5+} (0.565 Å) cations. The important bond-lengths are listed in Table S2 of the Supplemental Material [29]. It is evident from the table that the Ru-O bond-length lies in the range of 1.82–2.10 Å while Ca-O bond-length are in the range 2.20–2.24 Å. As a result of the difference in the bond lengths, the RuO_6 and CaO_6 octahedra are highly distorted. The average Ru-O bond length (~ 1.96 Å) is very close to that anticipated from sum of the ionic radii [30], while the average Ca-O bond-length (~ 2.21 Å) appears to be slightly shorter than expected. The Ru-O-Ru bond angles between the nearest-neighbor deviate significantly from the ideal 180° due to the octahedral tilting. The smallest Ru-Ru distance ~ 3.92 Å is formed via Ru-O bonds of very similar lengths (2.01 Å and 1.96 Å) while the longest Ru-Ru distance ~ 4.00 Å is formed via Ru-O bonds of significantly different lengths (2.10 Å and 1.94 Å). This Ru-Ru distance (~ 4.00 Å) is much larger than that observed in the $\text{Ba}_3\text{CaRu}_2\text{O}_9$ (~ 2.6 – 2.7 Å) which usually forms a Ru_2O_9 dimer of two face-sharing octahedra [14]. The corner-connected tilted RuO_6 octahedra form a unique buckled honeycomb lattice of Ru, where the distance between the two adjacent Ru atoms is ~ 4.00 Å. Such a buckled honeycomb lattice has also been observed in the related isostructural triple perovskites $\text{Sr}_3\text{CaIr}_2\text{O}_9$ and $\text{Sr}_3\text{CaOs}_2\text{O}_9$ [8,21].

Temperature dependence of zero-field cooled (ZFC) dc susceptibility $\chi(T)$ measured under the application of 1000 Oe and 100 Oe fields are depicted in Fig. 2(a) and Fig. S1 of the Supplemental Material [29], respectively. It exhibits an anomaly at Néel temperature $T_N \sim 190$ K associated with the long-range antiferromagnetic ordering of the Ru spins. This is further confirmed by our neutron diffraction studies. Below T_N , $\chi(T)$ decreases with decreasing temperature and shows a smeared broad anomaly ~ 160 K. On further decreasing the temperature, $\chi(T)$ shows an upturn below ~ 70 K and increases continuously down to the lowest temperature of measurements. A similar upturn has also been observed in the $\text{Ba}_3\text{CaRu}_2\text{O}_9$, $\text{Sr}_3\text{CaOs}_2\text{O}_9$ and attributed to the presence of trace amount of paramagnetic impurities [8]. Above T_N , the $\chi(T)$ is paramagnetic but it does not obey a Curie-Weiss behav-

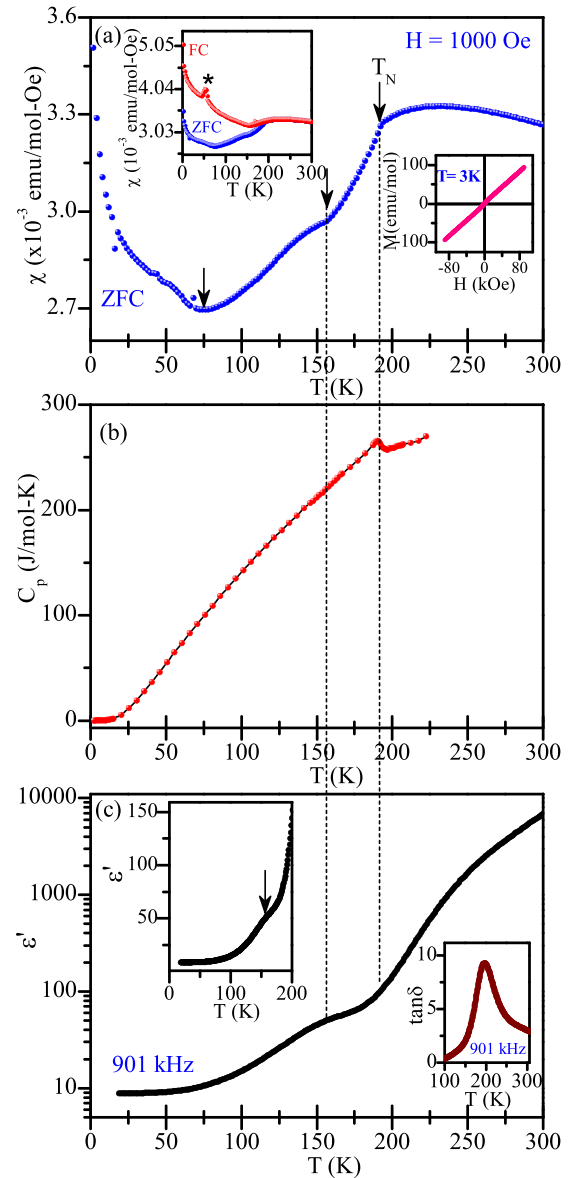


FIG. 2. Upper (a) Temperature-dependent dc susceptibility of $\text{Sr}_3\text{CaRu}_2\text{O}_9$ measured at 1000 Oe applied magnetic field under zero-field cooled protocol. The upper inset of (a) show the temperature dependence of ZFC and FC dc magnetic susceptibility measured at 1000 Oe. Asterisk marks the peak due to paramagnetic oxygen. The lower inset of (a) depicts the isothermal magnetization curve (M versus H) at 3.0 K. (b) Temperature-dependence of specific heat at zero-magnetic field. (c) Temperature dependence of real part of dielectric permittivity (ϵ') measured at 100 kHz frequency. The upper inset of (c) depicts the magnified view of ϵ' near the magnetic transition while the bottom inset shows the temperature dependence of loss tangent ($\tan\delta$) to clearly discern the anomaly across the long-range ordered antiferromagnetic transition.

ior. Consequently, it is not possible to estimate the strength of interaction, i.e., Curie-Weiss temperature, and effective magnetic moment. It is worth comparing the observed magnetic behavior of SCRO to other isostructural triple perovskites $\text{Sr}_3\text{CaIr}_2\text{O}_9$, $\text{Sr}_3\text{CaOs}_2\text{O}_9$. Despite having similar octahedral sharing of magnetic ions and bond lengths, bond angles, and direct Ir-Ir, Os-Os distances, the susceptibility of $\text{Sr}_3\text{CaIr}_2\text{O}_9$

displays a paramagneticlike behavior without any anomaly in the temperature range 2–300 K [21] whereas $\text{Sr}_3\text{CaOs}_2\text{O}_9$ is found to be ordered antiferromagnetic below $T_N \sim 385$ K [8]. Intriguingly, the occurrence of two magnetic transitions have also been observed in the family of Ba-based triple perovskite systems like $\text{Ba}_3\text{CoNb}_2\text{O}_9$ [31], $\text{Ba}_3\text{CoSb}_2\text{O}_9$ [32], $\text{Ba}_3\text{CoTa}_2\text{O}_9$ [33] and $\text{Ba}_3\text{MnNb}_2\text{O}_9$ [13] with a single magnetic ions at the B site. Notably, the magnetic transition temperatures of the above reported systems are much lower than that observed in our SCRO system.

The temperature dependence of both ZFC and field-cooled (FC) dc magnetic susceptibilities measured at 1000 Oe are compared in the upper inset of Fig. 2(a). It is evident that the FC χ (T) curve closely follows the ZFC χ (T) curve over a wide temperature range at higher temperatures but the two curves bifurcate significantly below $T_N \sim 190$ K, similar to other reported triple perovskites [7,18,34]. The bifurcation in ZFC and FC curve indicates the presence of glasslike state [35]. Below T_N , FC χ (T) curve decreases with decreasing temperature and shows an upturn around 160 K. This can happen as a precursor effect to an impending phase transition [36]. On further decreasing temperature, the FC χ (T) curve shows a peak/kink ~ 50 K. Such features have also been observed in other triple perovskites like $\text{Sr}_3\text{CaOs}_2\text{O}_9$ [8] and $\text{Ba}_3\text{CdIr}_2\text{O}_9$ [37] including $\text{Sr}_3\text{CaRu}_2\text{O}_9$ [8] and attributed to the paramagnetic oxygen contamination. Below 50 K, both ZFC and FC curves show increase in the susceptibility indicating a weak ferromagnetic behavior of SCRO at such low temperatures, as noted by previous authors also [8]. It is important to note that the FC χ (T) curve of SCRO reported by Thakur *et al.* [8] increases linearly below the upturn and saturates at low temperatures while in our case, the χ (T) curve increases gradually below the upturn and without any saturationlike behavior at low temperatures.

The isothermal M (H) hysteresis loop of SCRO at 3 K is shown in the lower inset of Fig. 2(a). It also reveals typical AFM behavior, i.e., linear M - H characteristic with a very small opening in the low field region (see Fig. S2 of the Supplemental Material [29] for more details). Such a small opening of the loop suggests the presence of a weak ferromagnetic component, possibly due to very small spin canting or defects. In contrast, Thakur *et al.* [8] report a weak ferromagneticlike M (H) hysteresis with a large coercive field $H_c \sim 10$ kOe and remanent magnetization $M_r \sim 50$ emu/mol in SCRO at 1.8 K. The large opening of the M (H) loop has been attributed to the presence of trace amount of ferromagnetic impurity, most probably SrRuO_3 [8].

The magnetic ordering in SCRO is further investigated by the specific heat (C_p) measurement, which is shown in (b) of Fig. 2. It is evident that the temperature dependence of C_p (T) exhibits a λ -like anomaly at $T_N \sim 190$ K. This again confirms the onset of long-range antiferromagnetic ordering consistent with dc susceptibility results. We also performed the analysis of the specific heat data and estimated the magnetic contribution to specific heat and entropy release at low temperatures (see Fig. S3 of the Supplemental Material [29] for more details). It is found that $C_m(T)$ follows a power law type temperature dependence: $C_m \propto T^\alpha$ with exponent $\alpha = (2.76 \pm 0.04)$. The value of exponent α is close to 3, expected for the long-range ordered antiferromagnetic

magnons [38]. A similar exponent has also been reported in the 6H-phase of $\text{Ba}_3\text{NiSb}_2\text{O}_9$ [39] and $\text{Ba}_2\text{Cu}_2\text{Te}_2\text{P}_2\text{O}_{13}$ [40] systems. Further, the presence of small entropy release at low temperatures suggests the possibility of a coexisting spin-glass phase with the long-range ordered antiferromagnetic phase [41]. The presence of spin-glass-like state in SCRO is also reflected in our ZFC and FC dc susceptibility measurements. Experimentally, the coexistence of long-range ordered and spin glass phases have been reported in several systems like $\text{Fe}_{(1-x)}\text{Mn}_x\text{TiO}_3$ [42], $\text{Fe}_{(1-x)}\text{Mg}_x\text{Cl}_2$ [43], multiferroic systems $\text{PbFe}_{1/2}\text{Nb}_{1/2}\text{O}_3$ [44,45], $(\text{Bi}_{1-x}\text{Ba}_x)(\text{Fe}_{1-x}\text{Ti}_x)\text{O}_3$ [46], site disordered kagome ferrite $\text{SrSn}_2\text{Fe}_4\text{O}_{11}$ [47], and pyrochlore antiferromagnet $\text{Na}_3\text{Co}(\text{CO}_3)_2\text{Cl}$ [48]. However, more experiments like ac susceptibility, memory effect and field-dependent specific heat would be required to fully establish the ground state of SCRO.

To get further insights into the nature of the observed anomalies, we plot the temperature dependence of real-part of dielectric permittivity (ϵ') at selected frequency of 901 kHz in Fig. 2(c). It has been reported that at such high frequencies (> 100 kHz), the extrinsic contribution to the dielectric permittivity is negligible [49]. We note that ϵ' increases monotonically with increasing temperature but exhibit two anomalies across the two magnetic transition. These anomalies are more clearly shown in the insets of Fig. 2(c). The temperature dependence of $\tan\delta$ exhibits a peak which coincides with the long-range ordering transition while a broad peak feature is also observed at the second magnetic transition of 160 K in the real part of ϵ' . The appearance of an anomaly in the $\epsilon'/\tan\delta$ across a magnetic transition is suggestive of magnetodielectric coupling [20]. We believe that our results may open an avenue to explore the magnetodielectric effects in the triple perovskite family which is scarcely investigated.

To get a microscopic understanding of the low-temperature magnetic transitions of SCRO, we carried out neutron powder diffraction (NPD) studies in the 250 to 1.5 K temperature range. Figure 3(a) displays the temperature-dependent evolution of NPD patterns over a selected range of time of flight (ToF) ~ 17 –85 ms (scattering angle = 58.3 deg and flight path length = 42.2 m) for SCRO. It is evident that no new peaks appear or disappear in the investigated temperature range 1.5 – 250 K. This implies that the crystal structure remains monoclinic in the $P2_1/c$ space group and that there is no structural phase transition in this temperature range. Moreover, around $T \approx 200$ K, we observed that the two Bragg peaks (~ 51.5 mToF and 27.5 mToF) start showing additional intensity contributions, which are due to the magnetic ordering of the Ru spins. The temperature evolution of the strongest magnetic peak after subtracting the 220 K pattern as a paramagnetic background is shown in Fig. 3(b), which clearly confirms the appearance of long-range ordered transition at $T_N \sim 200$ K. This is in close agreement with T_N observed in the dc susceptibility and specific heat measurements.

The temperature variation of the integrated intensity of the strongest magnetic peak (I_{mag}), containing two overlapping Bragg reflections (-111) and (-202), is shown in Fig. 3(c). Evidently, I_{mag} decreases with increasing temperature and completely disappears ~ 200 K. We have modeled the I_{mag} using a power law over a limited temperature range near T_N ($0.596 \leq T/T_N \leq 1$) [50]: $I(T) \propto (1 - T/T_N)^{2\beta}$, where T_N

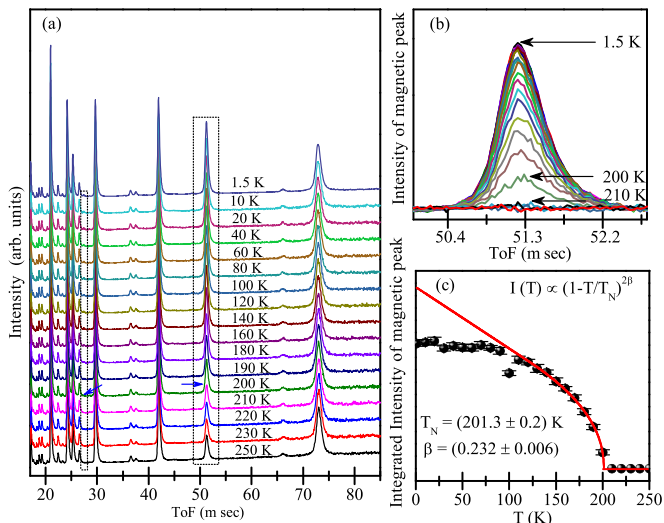


FIG. 3. (a) depicts the representative thermal evolution of neutron powder diffractogram of Sr₃CaRu₂O₉ recorded between 1.5 K to 250 K for 58° detector bank of WISH neutron diffractometer. (b) shows the temperature evolution of the strongest magnetic peak after subtraction of the 220 K pattern as a paramagnetic background. This clearly indicates the appearance of a magnetic peak around 200 K. (c) Variation of the integrated intensity of the strongest magnetic peak as a function of temperature. Solid line through data points represents the power law fit using the expression: $I(T) \propto (1-T/T_N)^{2\beta}$ with $T_N = (201.3 \pm 0.2)$ and $\beta = (0.232 \pm 0.006)$ which is close to that reported in the tricritical system.

and β represent the Néel temperature and critical exponent, respectively. The solid line through the data points is the best fit with $T_N = (201.3 \pm 0.2)$ K and $\beta = (0.232 \pm 0.006)$, respectively. It is interesting to note that the observed value of the critical exponent β is very close to that reported for a tricritical phase transition ($\beta = 0.25$) [51]. A similar exponent has also been reported in compounds like Cu₃Nb₂O₈ [50], (Ba_{1-x}Bi_x)(Ti_{1-x}Fe_x)O₃ [52] and EuAl₂Ge₂ [53].

The magnetic structure compatible with the monoclinic $P2_1/c$ space group symmetry is determined by representation analysis using the BasIreps program implemented in the FULLPROF suite [26]. The details of irreducible representations are given in Table S3 of the Supplemental Material [29]. The magnetic contribution superimposed on the nuclear Bragg contribution suggests the propagation vector $\mathbf{k} = (0\ 0\ 0)$. In the $P2_1/c$ space group with a monoclinic unit cell, Ru₁ and Ru₂ have the 4e site symmetry or on general positions. The reducible magnetic representation Γ can be decomposed in terms of four irreducible representations Γ_k for the 4e site as follows:

$$\Gamma(4e/Ru) = 3\Gamma_1^1 + 3\Gamma_2^1 + 3\Gamma_3^1 + 3\Gamma_4^1, \quad (1)$$

where Γ_1 , Γ_2 , Γ_3 and Γ_4 are one-dimensional in nature. Each irreps contains three basis vectors and, therefore, three refinable parameters.

We observed only two magnetic Bragg peaks in the NPD patterns of SCRO which is not sufficient to unambiguously solve the magnetic structure. In order to determine the magnetic structure and ordered moment of the Ru, we have made an assumption that the Ru ions on both sites have

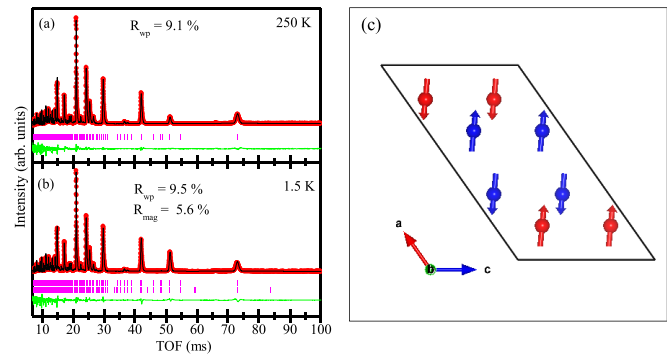


FIG. 4. Observed (filled circles), calculated (continuous line), and difference (bottom line) profiles obtained from Rietveld refinement using $P2_1/c$ space group at (a) 250 K and (b) 1.5 K. The vertical tick marks correspond to the position of all allowed Bragg reflections for the nuclear (top) and magnetic (bottom) reflections. Right shows the magnetic structure using Irrep Γ_2 . The Ru₁ and Ru₂ spins are shown with red and blue colors, respectively.

same magnetic moment. We have tested all four irreps against our NPD data. Out of four irreducible representations, Γ_1 and Γ_3 represent the ferromagnetic ordering with parallel arrangement of Ru spins and must be excluded according to susceptibility data. This leaves Γ_2 and Γ_4 as the likely representations for SCRO. The two representations can be distinguished by our Rietveld refinement analysis. The refinement corresponding to Γ_2 model reproduce the observed magnetic peak and gave the best fit with the lowest $R_{\text{Mag}} = 5.6\%$ at 1.5 K. The value of R_{Mag} for Γ_4 representation is nearly seven times larger than that of the Γ_2 model. The simultaneous refinement using Γ_2 model yields the magnetic moment $m_{\text{Ru}_1} = (1.77 \pm 0.04)\mu_B$ and $m_{\text{Ru}_2} = -(1.77 \pm 0.04)\mu_B$ at 1.5 K which is much smaller than the expected spin-only value of $3\mu_B$ for Ru⁵⁺. The observed value of the ordered moment is consistent with the many other reported Ru- and Os-based triple perovskite systems like Sr₃CaOs₂O₉ ($1.88(1)\mu_B$) [8], Ba₃LaRu₂O₉ ($1.4(1)\mu_B$) [10], Ba₃NiRu₂O₉ ($1.5(2)\mu_B$) [54,55], Ba₃CoRu₂O₉ ($1.44(5)\mu_B$) [54]. The strong suppression of the ordered moment in Ru-based systems has been attributed to a substantial hybridization effect between the Ru 4d and O 2p states [56]. Figures 4(a) and 4(b) depict the observed (filled circles), calculated (continuous line) and difference profiles obtained after Rietveld analysis of NPD data at 250 K (paramagnetic state) and 1.5 K (magnetically ordered state), respectively. The observed and calculated profiles show satisfactory fit as can be seen from the nearly flat difference profile. The corresponding magnetic structure of SCRO using Γ_2 model is shown in Fig. 4(c). The spins in the neighboring sites are coupled antiferromagnetically and lie in the ac plane. The Ru₁ and Ru₂ spins are shown with red and blue colors, respectively.

Even though there is no structural phase transition in SCRO down to 1.5 K, the temperature dependence of the monoclinic unit cell volume (see Fig. S4 and S5 of the Supplemental Material [29] for temperature variation of lattice parameters), as obtained from the Rietveld refinement analysis of NPD data shown in Fig. 5(a) reveals that the unit cell volume decreases linearly with decreasing temperature and shows a

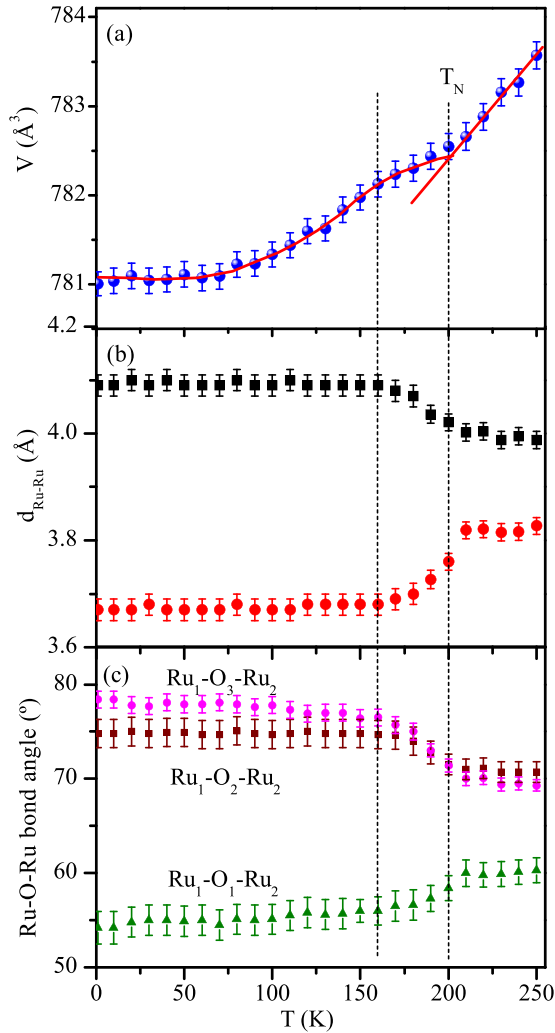


FIG. 5. Temperature dependence of (a) unit cell volume V , (b) direct Ru-Ru distance, and (c) Ru-O-Ru bond angles, as obtained by Rietveld refinement of NPD data of $\text{Sr}_3\text{CaRu}_2\text{O}_9$.

clear change of slope around 200 K followed by a smeared feature at the second transition ~ 160 K. The observation of an anomaly in the unit cell volume around the two magnetic transitions suggests magnetoelastic coupling [46]. Further, the temperature dependence of the direct Ru-Ru distance and some selected Ru-O-Ru bond angles are depicted in Figs. 5(b) and 5(c). Note that the both Ru-Ru distances are constant with decreasing temperatures up to the $T_N \sim 200$ K. On further decreasing temperature one of the Ru-Ru distance increases and other decreases gradually up to the second magnetic transition ~ 160 K and then constant down to the lowest temperature. The bond angles also change significantly across the T_N and increase/decrease up to 160 K. We believe that as a consequence of the monoclinic distortion, the multiple Ru-O-Ru bond angles (and bond lengths) are formed and thus creating multiple exchange interaction pathways that influence the magnetic properties of SCRO [11]. Thus our NPD analysis clearly reveals a significant change in the unit cell volume around the two transitions suggesting magnetoelastic coupling.

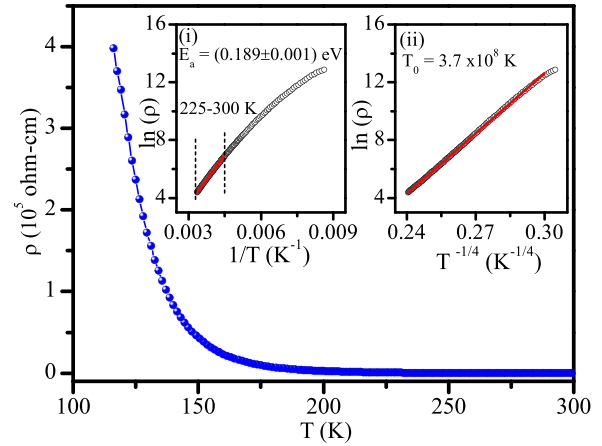


FIG. 6. Shows the temperature dependence of dc resistivity of $\text{Sr}_3\text{CaRu}_2\text{O}_9$. Inset: depict the plots corresponding to (i) simple Arrhenius model and (ii) Mott's variable-range hopping model. The solid lines through data points represent the fit for Eqs. (2) and (3), respectively.

Before going to next section, we would like to comment on the nature of the phase transition at 160 K. While there is no change of space group symmetry across the phase transition at $T \sim 160$ K, the direct Ru-Ru distance, bond-length, bond angles and unit cell volume change significantly across this transition. Such a change in the unit cell parameters and/or atomic distances without any change in the space group symmetry has previously been observed in systems like $\text{Co}_4\text{Nb}_2\text{O}_9$ [57], rare-earth hexagonal manganites RMnO_3 ($R = \text{Lu}, \text{Y}$) [58] and BiFeO_3 -based solid solutions [46,49] where it has been attributed to an isostructural phase transition driven by spin-phonon coupling. We believe that the phase transition at 160 K in SCRO is due to an isostructural phase transition. However, temperature dependent Raman scattering studies are required to understand the origin of this transition.

The temperature dependence of the electrical resistivity (ρ) of SCRO at zero magnetic fields is shown in Fig. 6. It is evident that the $\rho(T)$ increases with decreasing temperature indicating the insulating nature of the SCRO. Below 116 K, $\rho(T)$ goes beyond the measurement limit of the PPMS instrument. The value of resistivity increased several orders of magnitude at 116 K ($\rho \sim 4 \times 10^5$ ohm-cm) as compared to the room temperature resistivity ($\rho \sim 81$ ohm-cm). To understand the transport mechanism, we attempted to fit the data to the Arrhenius law described by

$$\rho = \rho_0 \exp(E_a/k_B T), \quad (2)$$

where ρ_0 is a constant, E_a is the activation energy and k_B is the Boltzmann constant. As per Arrhenius Eq. (2), the $\ln(\rho)$ versus $1/T$ plot should be linear. The Arrhenius plot shown in the inset (i) of Fig. 6 exhibits linear behavior only in the limited range 225–300 K and deviates very significantly at low temperatures which possibly suggests a three-dimensional (3D) variable range hopping (VRH) mechanism [59]. The activation energy estimated from the fitting of the linear region comes out to be $E_a \sim 0.189$ eV. This is in close agreement with the E_a determined from the temperature-dependent dielectric study. Further, we attempted to fit Mott's 3D VRH

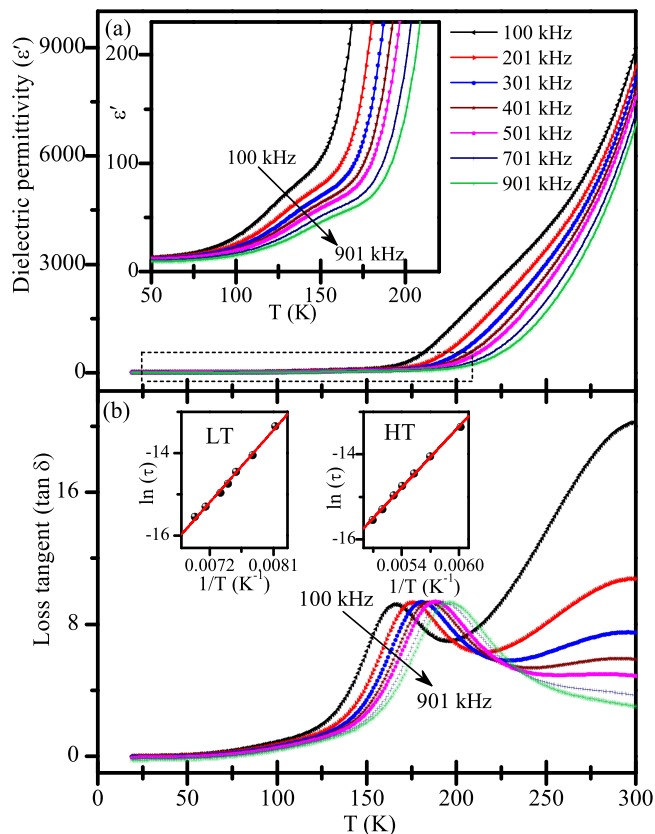


FIG. 7. Temperature dependence of (a) real part of dielectric permittivity (ϵ') and (b) loss tangent ($\tan \delta$) at different frequencies for $\text{Sr}_3\text{CaRu}_2\text{O}_9$. Inset of (a) depicts the variation of dielectric permittivity on a magnified scale for LT transition. Insets of (b) show the $\ln(\tau)$ versus $1/T$ plots for LT and HT transition. Solid lines through data points represent the least-squares fit to the Arrhenius law as described in the text.

model described by [59]

$$\rho(T) = \rho_0[\exp(T_0/T)]^{1/4}, \quad (3)$$

where T_0 is the Mott's activation energy (in units of temperature) which depends on the density of states at the Fermi level [$N(E_F)$] and localization length (ξ) through a relation ($T_0 \propto 1/N(E_F)\xi^3$). The linear nature of the $\ln(\rho)$ versus $T^{-1/4}$ plot in almost the entire temperature range [see the inset (ii) of Fig. 6] suggest that the transport mechanism of charge carriers in SCRO is well described by the 3D VRH model. This is similar to what is reported in the double perovskites $\text{Sr}_2\text{CoRuO}_6$ [60], $\text{Ca}_{2-x}\text{Sr}_x\text{FeRuO}_6$ [61] and triple perovskites $\text{Sr}_3\text{CaOs}_2\text{O}_9$ [8], $\text{Sr}_3\text{CaIr}_2\text{O}_9$ [21], and $\text{Ba}_3\text{NiIr}_2\text{O}_9$ [3]. The observed value of $T_0 = 3.7 \times 10^8$ K is in line with reported values for other Ru-based oxides [60,62].

Figure 7 presents the temperature dependence of the real part of dielectric permittivity (ϵ') and loss tangent ($\tan \delta$) at several frequencies ranging from 100 kHz–901 kHz. It is notable that the $\text{Sr}_3\text{CaRu}_2\text{O}_9$ exhibits a large ϵ' at room temperature ($\epsilon' \sim 8600$ at 100 kHz) similar to that reported in the well-known relaxor ferroelectriclike materials $\text{Pb}(\text{Mg}_{1/3}\text{Nb}_{2/3})\text{O}_3$ [63], $\text{Pb}(\text{Mg}_{1/3}\text{Nb}_{2/3})\text{O}_3$ – PbTiO_3 [64]. We observe two distinct frequency dispersions near the

magnetic transitions in the ϵ' - T plot. These two frequency dispersions hereafter labeled as low-temperature (LT) and high-temperature (HT), suggest the presence of two dielectric relaxations in SCRO. In addition, the $\tan \delta$ exhibits a peak at the inflection point of the ϵ' at a particular frequency for the HT relaxation. We note that the peak position of $\tan \delta$ shifts to higher temperature side with increasing frequency. The first derivative of ϵ' (i.e., $d\epsilon'/dT$) was used to determine the accurate peak position for the analysis of LT relaxation while the HT relaxation is analyzed by the $\tan \delta$ peak at the inflection point of ϵ' . The relaxation time ($\tau = 1/2\pi f$) corresponding to both peak temperatures follow simple Arrhenius behavior [$\tau = \tau_0 \exp(E_a/k_B T)$], as can be seen from the linear nature of the $\ln(\tau)$ versus $1/T$ plot [see the insets of the lower (b) in Fig. 7]. The activation energy and relaxation time obtained from the straight-line fit are: $E_a^{\text{LT}} = (0.167 \pm 0.004)$ eV, $\tau_0^{\text{LT}} = (2.1 \pm 0.6) \times 10^{-13}$ s and $E_a^{\text{HT}} = (0.203 \pm 0.002)$ eV, $\tau_0^{\text{HT}} = (7.5 \pm 2) \times 10^{-13}$ s, respectively, for the LT and HT dielectric relaxations. The observed value of E_a is comparable to the values reported for polaronic relaxation in the range $E_a = 0.14 - 0.28$ eV caused by charge carrier hopping [65–69]. It is interesting to note that the observed peak temperatures nearly coincide with the magnetic transition temperatures suggesting that the charge and spin degrees of freedom are coupled and hint towards the possibility of magnetodielectric coupling in SCRO. However, further field-dependent experiments would be required to confirm the magnetodielectric effect in SCRO.

IV. CONCLUSIONS

In summary, we have presented temperature-dependent structure, magnetic, dielectric, and transport properties of the ordered triple perovskite system $\text{Sr}_3\text{CaRu}_2\text{O}_9$. Stabilizing in the monoclinic $P2_1/c$ symmetry at room temperature. We observe successive magnetic phase transitions ~ 190 and ~ 160 K in the dc susceptibility studies. A clear λ -like anomaly at 190 K in specific heat confirms the true thermodynamic nature of the para-antiferromagnetic phase transition. Temperature-dependent neutron powder diffraction measurements rule out within instrumental resolution, the possibility of a structural transition, and the system remains in the monoclinic $P2_1/c$ symmetry down to 1.5 K. Interestingly, the integrated intensity of the magnetic peak (I_{mag}) decreases continuously with increasing temperature and vanishes around 200 K. We have modeled the temperature variation of I_{mag} using the power law type functional dependence $I(T) \propto (1-T/T_N)^{2\beta}$ with critical exponent $\beta = (0.232 \pm 0.006)$ and $T_N = (201.3 \pm 0.2)$ K, respectively. Our results show that the unit cell volume, direct Ru-Ru distance, bond angles and dielectric permittivity/loss tangent change significantly across the magnetic transitions suggesting the presence of magnetoelastic and magnetodielectric couplings, respectively.

ACKNOWLEDGMENTS

A.K. acknowledges SERB-DST, Government of India and I-HUB Quantum Technology Foundation Pune for providing

financial support through a Post-Doctoral Fellowship (PDF/2020/002116). Authors acknowledge S. Kumar for his

help in sample synthesis. S.N. acknowledges support from an Air Force Research Laboratory Grant (FA2386-21-1-4051).

- [1] J. G. Rau, E. K. H. Lee, and H. Y. Kee, Spin-orbit physics giving rise to novel phases in correlated systems: Iridates and related materials, *Annu. Rev. Condens. Matter Phys.* **7**, 195 (2016).
- [2] T. Dey, R. Kumar, A. V. Mahajan, S. D. Kaushik, and V. Siruguri, Unconventional magnetism in the spin-orbit-driven mott insulators $\text{Ba}_3\text{MIR}_2\text{O}_9$ ($M = \text{Sc, Y}$), *Phys. Rev. B* **89**, 205101 (2014).
- [3] S. Kumar, S. K. Panda, M. M. Patidar, S. K. Ojha, P. Mandal, G. Das, J. W. Freeland, V. Ganesan, P. J. Baker, and S. Middey, Spin-liquid behavior of the three-dimensional magnetic system $\text{Ba}_3\text{NiIr}_2\text{O}_9$ with $S = 1$, *Phys. Rev. B* **103**, 184405 (2021).
- [4] H. D. Zhou, E. S. Choi, G. Li, L. Balicas, C. R. Wiebe, Y. Qiu, J. R. D. Copley, and J. S. Gardner, Spin liquid state in the $S = 1/2$ triangular lattice $\text{Ba}_3\text{CuSb}_2\text{O}_9$, *Phys. Rev. Lett.* **106**, 147204 (2011).
- [5] S. Kundu *et al.*, Gapless quantum spin liquid in the triangular system $\text{Sr}_3\text{CuSb}_2\text{O}_9$, *Phys. Rev. Lett.* **125**, 267202 (2020).
- [6] A. Nag, S. Middey, S. Bhowal, S. K. Panda, R. Mathieu, J. C. Orain, F. Bert, P. Mendels, P. G. Freeman, M. Mansson *et al.*, Origin of the spin-orbital liquid state in a nearly $J = 0$ iridate $\text{Ba}_3\text{ZnIr}_2\text{O}_9$, *Phys. Rev. Lett.* **116**, 097205 (2016).
- [7] S. Gondh, M. M. Patidar, K. Kumar, M. P. Saravanan, V. Ganesan, and A. K. Pramanik, Large exchange bias and low-temperature glassy state in the frustrated triangular-lattice antiferromagnet $\text{Ba}_3\text{NiIr}_2\text{O}_9$, *Phys. Rev. B* **104**, 014401 (2021).
- [8] G. S. Thakur, T. C. Hansen, W. Schnelle, S. Guo, O. Janson, J. Van Den Brink, C. Felser, and M. Jansen, Buckled honeycomb lattice compound $\text{Sr}_3\text{CaOs}_2\text{O}_9$ exhibiting antiferromagnetism above room temperature, *Chem. Mater.* **34**, 4741 (2022).
- [9] H. D. Zhou, A. Kiswandhi, Y. Barlas, J. S. Brooks, T. Siegrist, G. Li, L. Balicas, J. G. Cheng, and F. Rivadulla, Orbital, charge, and spin couplings in $\text{Ru}_2^{5+}\text{O}_9$ dimers of $\text{Ba}_3\text{CoRu}_2\text{O}_9$, *Phys. Rev. B* **85**, 041201(R) (2012).
- [10] M. S. Senn, S. A. J. Kimber, A. M. Arevalo Lopez, A. H. Hill, and J. P. Attfield, Spin orders and lattice distortions of geometrically frustrated 6H-perovskites $\text{Ba}_3\text{B}'\text{Ru}_2\text{O}_9$ ($\text{B}' = \text{La}^{3+}, \text{Nd}^{3+}, \text{and Y}^{3+}$), *Phys. Rev. B* **87**, 134402 (2013).
- [11] A. Nag *et al.*, $\text{Ba}_3\text{MIR}_2\text{O}_9$ hexagonal perovskites in the light of spin-orbit coupling and local structural distortions, *Phys. Rev. B* **97**, 064408 (2018).
- [12] J. Hwang, E. S. Choi, F. Ye, C. R. Dela Cruz, Y. Xin, H. D. Zhou, and P. Schlottmann, Successive magnetic phase transitions and multiferroicity in the spin-one triangular-lattice antiferromagnet $\text{Ba}_3\text{NiNb}_2\text{O}_9$, *Phys. Rev. Lett.* **109**, 257205 (2012).
- [13] M. Lee, E. S. Choi, X. Huang, J. Ma, C. R. Dela Cruz, M. Matsuda, W. Tian, Z. L. Dun, S. Dong, and H. D. Zhou, Magnetic phase diagram and multiferroicity of $\text{Ba}_3\text{MnNb}_2\text{O}_9$: A SPIN-5/2 triangular lattice antiferromagnet with weak easy-axis anisotropy, *Phys. Rev. B* **90**, 224402 (2014).
- [14] M. S. Senn, A. M. Arevalo-Lopez, T. Saito, Y. Shimakawa, and J. Paul Attfield, Nonmagnetic spin-singlet dimer formation and coupling to the lattice in the 6h perovskite $\text{Ba}_3\text{CaRu}_2\text{O}_9$, *J. Phys. Condens. Matter* **25**, 496008 (2013).
- [15] W. Müller, M. Avdeev, Q. Zhou, A. J. Studer, B. J. Kennedy, G. J. Kearley, and C. D. Ling, Spin-gap opening accompanied by a strong magnetoelastic response in the $S = 1$ magnetic dimer system $\text{Ba}_3\text{BiRu}_2\text{O}_9$, *Phys. Rev. B* **84**, 220406(R) (2011).
- [16] W. Müller *et al.*, Giant magnetoelastic effect at the opening of a spin-gap in $\text{Ba}_3\text{BiIr}_2\text{O}_9$, *J. Am. Chem. Soc.* **134**, 3265 (2012).
- [17] S. A. J. Kimber, M. S. Senn, S. Fratini, H. Wu, A. H. Hill, P. Manuel, J. P. Attfield, D. N. Argyriou, and P. F. Henry, Charge order at the frontier between the molecular and solid states in $\text{Ba}_3\text{NaRu}_2\text{O}_9$, *Phys. Rev. Lett.* **108**, 217205 (2012).
- [18] C. Garg, D. Roy, M. Lonsky, P. Manuel, A. Cervellino, J. Müller, M. Kabir, and S. Nair, Evolution of the structural, magnetic, and electronic properties of the triple perovskite $\text{Ba}_3\text{CoIr}_2\text{O}_9$, *Phys. Rev. B* **103**, 014437 (2021).
- [19] T. Basu, A. Pautrat, V. Hardy, A. Loidl, and S. Krohns, Magnetodielectric coupling in a Ru-based 6H-perovskite, $\text{Ba}_3\text{NdRu}_2\text{O}_9$, *Appl. Phys. Lett.* **113**, 042902 (2018).
- [20] T. Basu, V. Caignaert, S. Ghara, X. Ke, A. Pautrat, S. Krohns, A. Loidl, and B. Raveau, Enhancement of magnetodielectric coupling in 6H-perovskites $\text{Ba}_3\text{RRu}_2\text{O}_9$ for heavier rare-earth cations ($R = \text{Ho, Tb}$), *Phys. Rev. Mater.* **3**, 114401 (2019).
- [21] D. C. Wallace and T. M. McQueen, New Honeycomb Iridium (V) Oxides: NaIrO_3 and $\text{Sr}_3\text{CaIr}_2\text{O}_9$, *Dalt. Trans.* **44**, 20344 (2015).
- [22] V. Primo-Martín and M. Jansen, Synthesis, structure, and physical properties of cobalt perovskites: $\text{Sr}_3\text{CoSb}_2\text{O}_9$ and $\text{Sr}_2\text{CoSbO}_{6-\delta}$, *J. Solid State Chem.* **157**, 76 (2001).
- [23] J. T. Rijssenbeek, S. Malo, V. Caignaert, and K. R. Poeppelmeier, Site and oxidation-state specificity yielding dimensional control in perovskite ruthenates, *J. Am. Chem. Soc.* **124**, 2090 (2002).
- [24] M. W. Lufaso, Crystal structures, modeling, and dielectric property relationships of 2:1 ordered $\text{Ba}_3\text{MM}'_2\text{O}_9$ ($M = \text{Mg, Ni, Zn}$; $M' = \text{Nb, Ta}$) perovskites, *Chem. Mater.* **16**, 2148 (2004).
- [25] L. C. Chapon, P. Manuel, P. G. Radaelli, C. Benson, S. Ansell, N. J. Rhodes, D. Raspino, D. Duxbury, E. Spill, and J. Norris, Wish: The new powder and single crystal magnetic diffractometer on the second target station, *Neutron News* **22**, 22 (2011).
- [26] J. Rodriguez-Carvajal, Introduction to the Program FULLPROF: Refinement of crystal and magnetic structures from powder and single crystal data (2001).
- [27] K. Momma and F. Izumi, VESTA 3 for three-dimensional visualization of crystal, volumetric and morphology data, *J. Appl. Crystallogr.* **44**, 1272 (2011).
- [28] G. Caglioti, A. Paoletti, and F. P. Ricci, Choice of collimators for a crystal spectrometer for neutron diffraction, *Nucl. Instruments* **3**, 223 (1958).
- [29] See Supplemental Material at <http://link.aps.org/supplemental/10.1103/PhysRevMaterials.8.024405> for details of refined structural parameters, selected bond distances, field dependent dc magnetic susceptibility, M-H curve at 3 K, specific heat analysis and variation of unit cell parameters as a function of temperature.

- [30] R. D. Shannon, Revised effective ionic radii and systematic studies of interatomic distances in halides and chalcogenides, *Acta Crystallogr.* **A32**, 751 (1976).
- [31] M. Lee, J. Hwang, E. S. Choi, J. Ma, C. R. Dela Cruz, M. Zhu, X. Ke, Z. L. Dun, and H. D. Zhou, Series of phase transitions and multiferroicity in the quasi-two-dimensional spin-1/2 triangular-lattice antiferromagnet $\text{Ba}_3\text{CoNb}_2\text{O}_9$, *Phys. Rev. B* **89**, 104420 (2014).
- [32] H. D. Zhou *et al.*, Successive phase transitions and extended spin-excitation continuum in the $S = 1/2$ triangular-lattice antiferromagnet $\text{Ba}_3\text{CoSb}_2\text{O}_9$, *Phys. Rev. Lett.* **109**, 267206 (2012).
- [33] K. M. Ranjith, K. Brinda, U. Arjun, N. G. Hegde, and R. Nath, Double phase transition in the triangular antiferromagnet $\text{Ba}_3\text{CoTa}_2\text{O}_9$, *J. Phys. Condens. Matter* **29**, 115804 (2017).
- [34] T. Ferreira, D. Carone, A. Huon, A. Herklotz, S. A. Stoian, S. M. Heald, G. Morrison, M. D. Smith, and H. Loye, $\text{Ba}_3\text{Fe}_{1.56}\text{Ir}_{1.44}\text{O}_9$: A polar semiconducting triple perovskite with near room temperature magnetic ordering, *Inorg. Chem.* **57**, 7362 (2018).
- [35] E. Vincent and V. Dupuis, Spin glasses: Experimental signatures and salient outcomes, *Springer Ser. Mater. Sci.* **275**, 31 (2018).
- [36] A. Kumar, P. Singh, R. J. Choudhary, and D. Pandey, Effect of Mn-doping on the low temperature magnetic phase transitions of BiFeO_3 , *J. Alloys Compd.* **825**, 154148 (2020).
- [37] M. S. Khan, A. Bandyopadhyay, A. Nag, V. Kumar, A. V. Mahajan, and S. Ray, Magnetic ground state of the distorted 6H perovskite $\text{Ba}_3\text{CdIr}_2\text{O}_9$, *Phys. Rev. B* **100**, 064423 (2019).
- [38] E. S. R. Gopal, *Specific Heat at Low Temperatures*, 1st ed. (Springer, New York, 1966).
- [39] J. G. Cheng, G. Li, L. Balicas, J. S. Zhou, J. B. Goodenough, C. Xu, and H. D. Zhou, High-pressure sequence of $\text{Ba}_3\text{NiSb}_2\text{O}_9$ structural phases: New $S = 1$ quantum spin liquids based on Ni^{2+} , *Phys. Rev. Lett.* **107**, 197204 (2011).
- [40] V. Kumar, A. Shahee, S. Kundu, M. Baenitz, and A. V. Mahajan, Spin-1/2 chain compound $\text{Ba}_2\text{Cu}_2\text{Te}_2\text{P}_2\text{O}_{13}$: Magnetization, specific heat, and local-probe NMR, *Phys. Rev. B* **102**, 104419 (2020).
- [41] K. Binder and A. P. Young, Spin glasses: Experimental facts, theoretical concepts, and open questions, *Rev. Mod. Phys.* **58**, 801 (1986).
- [42] H. Yoshizawa, S. Mitsuda, H. Aruga, and A. Ito, Mixed phase of spin-glass ordering and antiferromagnetism in an Ising system, $\text{Fe}_x\text{Mn}_{1-x}\text{TiO}_3$, *Phys. Rev. Lett.* **59**, 2364 (1987).
- [43] P. Z. Wong, S. Von Molnar, T. T. M. Palstra, J. A. Mydosh, H. Yoshizawa, S. M. Shapiro, and A. Ito, Coexistence of spin-glass and antiferromagnetic orders in the Ising system $\text{Fe}_{0.55}\text{Mg}_{0.45}\text{Cl}_2$, *Phys. Rev. Lett.* **55**, 2043 (1985).
- [44] W. Kleemann, V. V. Shvartsman, P. Borisov, and A. Kania, Coexistence of antiferromagnetic and spin cluster glass order in the magnetoelectric relaxor multiferroic $\text{PbFe}_{0.5}\text{Nb}_{0.5}\text{O}_3$, *Phys. Rev. Lett.* **105**, 257202 (2010).
- [45] S. Chillal, M. Thede, F. J. Litterst, S. N. Gvasaliya, T. A. Shaplygina, S. G. Lushnikov, and A. Zheludev, Microscopic coexistence of antiferromagnetic and spin-glass states, *Phys. Rev. B* **87**, 220403(R) (2013).
- [46] A. Kumar, S. D. Kaushik, V. Siruguri, and D. Pandey, Evidence for two spin-glass transitions with magnetoelastic and magnetolectric couplings in the multiferroic $(\text{Bi}_{1-x}\text{Ba}_x)(\text{Fe}_{1-x}\text{Ti}_x)\text{O}_3$ system, *Phys. Rev. B* **97**, 104402 (2018).
- [47] L. Shlyk, S. Strobel, B. Farmer, L. E. De Long, and R. Niewa, Coexistence of ferromagnetism and unconventional spin-glass freezing in the site-disordered kagome ferrite $\text{SrSn}_2\text{Fe}_4\text{O}_{11}$, *Phys. Rev. B* **97**, 054426 (2018).
- [48] Z. Fu, Y. Zheng, Y. Xiao, S. Bedanta, A. Senyshyn, G. G. Simeoni, Y. Su, U. Rücker, P. Kögerler, and T. Brückel, Coexistence of magnetic order and spin-glasslike phase in the pyrochlore antiferromagnet $\text{Na}_3\text{Co}(\text{CO}_3)_2\text{Cl}$, *Phys. Rev. B* **87**, 214406 (2013).
- [49] A. Singh, V. Pandey, R. K. Kotnala, and D. Pandey, Direct evidence for multiferroic magnetoelectric coupling in $0.9\text{BiFeO}_3-0.1\text{BaTiO}_3$, *Phys. Rev. Lett.* **101**, 247602 (2008).
- [50] R. D. Johnson, S. Nair, L. C. Chapon, A. Bombardi, C. Vecchini, D. Prabhakaran, A. T. Boothroyd, and P. G. Radaelli, $\text{Cu}_3\text{Nb}_2\text{O}_8$: A multiferroic with chiral coupling to the crystal structure, *Phys. Rev. Lett.* **107**, 137205 (2011).
- [51] E. K. H. Salje, *Phase Transitions in Ferroelastic and Co-Elastic Crystals* (Cambridge University Press, Cambridge, 1990).
- [52] A. Singh, C. Moriyoshi, Y. Kuroiwa, and D. Pandey, Evidence for diffuse ferroelectric phase transition and cooperative tricritical freezing of random site dipoles due to off-centered Bi^{3+} ions in the average cubic lattice of $(\text{Ba}_{1-x}\text{Bi}_x)(\text{E}_{1-x}\text{Fe}_x)\text{O}_3$, *Phys. Rev. B* **85**, 064116 (2012).
- [53] S. Pakhira *et al.*, Anisotropic magnetism and electronic structure of trigonal EuAl_2Ge_2 single crystals, *Phys. Rev. B* **107**, 134439 (2023).
- [54] P. Lightfoot and P. D. Battle, The crystal and magnetic structures of $\text{Ba}_3\text{NiRu}_2\text{O}_9$, $\text{Ba}_3\text{CoRu}_2\text{O}_9$ and $\text{Ba}_3\text{ZnRu}_2\text{O}_9$, *J. Solid State Chem.* **89**, 174 (1990).
- [55] J. T. Rijssenbeek, Q. Huang, R. W. Erwin, H. W. Zandbergen, and R. J. Cava, The crystal structure of $\text{Ba}_3\text{CuRu}_2\text{O}_9$ and comparison to $\text{Ba}_3\text{MRu}_2\text{O}_9$ ($M = \text{In}, \text{Co}, \text{Ni}, \text{and Fe}$), *J. Solid State Chem.* **146**, 65 (1999).
- [56] S. V. Streltsov, Magnetic moment suppression in $\text{Ba}_3\text{CoRu}_2\text{O}_9$: Hybridization effect, *Phys. Rev. B* **88**, 024429 (2013).
- [57] R. Jana, A. B. Garg, B. Joseph, B. Chakraborty, K. A. Irshad, and R. Rao, Pressure-induced multiple phase transitions in the magnetoelectric $\text{Co}_4\text{Nb}_2\text{O}_9$, *Phys. Rev. B* **108**, 115107 (2023).
- [58] S. Lee *et al.*, Giant magnetoelastic coupling in multiferroic hexagonal manganites, *Nature (London)* **451**, 805 (2008).
- [59] N. F. Mott and E. A. Davis, *Electronic Processes in Non-Crystalline Materials* (Clarendon, Oxford, 1979).
- [60] R. Phatak, K. Krishnan, S. K. Sali, A. Das, and A. K. Nigam, Structure and magnetic properties of $\text{Sr}_2\text{CoRuO}_6$, *J. Magn. Mater.* **344**, 129 (2013).
- [61] K. Naveen *et al.*, Reentrant magnetism at the borderline between long-range antiferromagnetic order and spin-glass behavior in the B site disordered perovskite system $\text{Ca}_{2-x}\text{Sr}_x\text{FeRuO}_6$, *Phys. Rev. B* **98**, 224423 (2018).
- [62] J. G. Bos and J. P. Attfield, Structural, magnetic, and transport properties of $(\text{La}_{1+x}\text{Sr}_{1-x})\text{CoRuO}_6$ double perovskites, *Chem. Mater.* **16**, 1822 (2004).
- [63] R. A. Cowley, S. N. Gvasaliya, S. G. Lushnikov, B. Roessli, and G. M. Rotaru, Relaxing with relaxors: A review of relaxor ferroelectrics, *Adv. Phys.* **60**, 229 (2011).

- [64] E. Sun and W. Cao, Relaxor-based ferroelectric single crystals: Growth, domain engineering, characterization and applications, *Prog. Mater. Sci.* **65**, 124 (2014).
- [65] A. Kumar, G. Sahu, and S. Nair, Evidence for cluster glass ground state in the potential giant dielectric constant material $\text{Ba}(\text{Fe}_{1/2}\text{Sn}_{1/2})\text{O}_{3-\delta}$, *J. Alloys Compd.* **920**, 165914 (2022).
- [66] Q. Ke, X. Lou, Y. Wang, and J. Wang, Oxygen-vacancy-related relaxation and scaling behaviors of $\text{Bi}_{0.9}\text{La}_{0.1}\text{Fe}_{0.98}\text{Mg}_{0.02}\text{O}_3$ ferroelectric thin film, *Phys. Rev. B* **82**, 024102 (2010).
- [67] R. Ahmed, S. T. Wang, J. Sun, J. Wang, T. Y. Li, Y. Yu, Q. J. Li, and C. C. Wang, Colossal dielectric behavior in $\text{BaFeO}_{3-\delta}$ ceramics, *Ceram. Int.* **45**, 13484 (2019).
- [68] C. Chen, K. B. Xu, Y. M. Cui, and C. C. Wang, Polaronic relaxation in LaFeO_3 , *Mater. Lett.* **89**, 153 (2012).
- [69] A. Kumar and G. Sahu, The magnetic ground state of $\text{Ba}(\text{Fe}_{1/2}\text{Sn}_{1/2})\text{O}_{3-\delta}$: A potential giant dielectric material for technological applications, *J. Alloys Compd.* **961**, 171003 (2023).